Int J Adv Manuf Technol (2017) 90:1131–1143
DOI 10.1007/s00170-016-9430-6

ORIGINAL ARTICLE

Numerical and experimental study on the effects of welding environment and input heat on properties of FSSWed TRIP steel

Amir Mostafapour [1] · **Ali Ebrahimpour** [1] · **Tohid Saeid** [2]

Received: 4 June 2016 / Accepted: 31 August 2016 / Published online: 19 September 2016

Abstract In this paper, the effect of input heat and welding environment on microstructure and mechanical properties of friction stir spot welded TRIP steel sheets were investigated. Six types of joints produced in both air and water environments and under rotational speeds of 900, 1350, and 1800 rpm. Then, the microstructure and mechanical properties of them were studied. The thermal histories, strain, and strain rate distributions of cases obtained by finite element modeling. According to the temperature and strain distribution and microstructural observations, four different zones determined in welding region: stir zone, thermomechanically affected zone, and high and low temperature heat-affected zones. It is obtained at in-air welds by increasing the rotational speed, the strength of joints increase to a maximum value because of higher strain rate and more recrystallization of prior austenite grains. The strength then decreases due to high amount of heat input and growth of recrystallized grains. Thermal history of underwater welds showed lower peak temperature and rapid cooling rate. Also, by increasing rotational speed in underwater joints, the strength and hardness increased because of microstructure refinement. The fracture surfaces of joints showed a dimple pattern ductile fracture in all cases except 1800 rpm in-air joint that the fracture was less ductile which agrees with lower tensile elongation of it.

Keywords Friction stir spot welding · Finite element modeling · TRIP steel · Underwater welding · Input heat

1 Introduction

There is an increasing interest concerning the application of transformation-induced plasticity (TRIP) steels in automotive industry because of their good combination of high strength and formability due to the existence of retained austenite in their microstructures, which transforms to the martensite phase during deformation [1]. The microstructure of TRIP steels is obtained by alloying, usually with C, Mn, Al, and Si, and a two-stepped heat treatment, resulting in ferrite, bainite, and retained austenite [2].

According to the application of TRIP steels in automotive industry, there is an increasing demand to joining them. Unfortunately, the fusion welding processes destroy the initial microstructure, and therefore, decrease the related strength and ductility [3].

Friction stir spot welding (FSSW) base on fundamentals of FSW [4] as a new spot welding method can be used to join overlapping workpieces and proposes to replace the resistance spot welding. This method consists of only the plunge, dwell, and retract stages of FSW [5]. Because of the solid-state nature of the FSSW process, the peak temperature during the FSSW thermal cycle is remarkably lower than the melting point of metals, thereby, restricting the formation of the coarse grains and the detrimental solidification defects. Therefore, the higher strength and toughness would be yielded in the FSSW joints.

There are numerous studies that have investigated the FSSW of steels [6–8], but studies about FSSW of TRIP steels are very limited [3, 9]. In one of them, Lomholt et al. [3] investigated FSSW of TRIP690 steel and reported that

---

✉ Ali Ebrahimpour
aliebrahimpour414@gmail.com

[1] Faculty of Mechanical Engineering, University of Tabriz, Tabriz, Iran

[2] Faculty of Materials Engineering, Sahand University of Technology, Tabriz, Iran

FSSW is suitable to produce successful welds in this type of TRIP steel. The best weld parameters obtained with 1500 rpm rotational speed and 1 s dwell time, which was confirmed by the highest shear tension strength and a distinctive hardness profile.

It is reported [10] that FSW includes complex interactions between a variety of simultaneous thermomechanical processes which affect the heating and cooling rates, deformation, recrystallization, and the mechanical properties of the joint. Also, He et al. [11] mentioned that the unsuitable selection of the FSW parameters arrives to an unusually high gradient of temperature, strain, and strain rate. Therefore, the obtained microstructures typically show an intense variation in the morphology and grain size. In the other study, Heidarzadeh et al. [12] reported that by increasing input heat during FSW, the mechanical properties of the joint reduce because of grain growth. Because of these problems, the full potential of FSW/FSSW for improving the mechanical properties by microstructural refinement cannot be used. Therefore, in recent years, there is an increasing interest to control of thermal history of FSWed joints by controlling welding environment [13–16]. Rouhi et al. [13] investigated the effects of welding environment on microstructure and mechanical properties of friction stir welded AZ91C magnesium alloy joints. The results indicated that the tensile strength of the underwater joint was higher than that of the normal joint, confirming the feasibility of underwater FSW to improve the joint properties. Also, Imam et al. [14] studied the effect of online rapid cooling via liquid CO_2 during FSW of medium carbon steel and reported that refinement of stir zone increase by using rapid cooling and so the mechanical properties of joint improve.

On the other hand, because the measurement of the thermomechanical parameters during FSW/FSSW is very difficult, costly, and time consuming, very limited experimental studies exist on thermal history and strain in FSW/FSSW [17–19], and many of the authors have used simulation methods in this regard. He et al. [11] have provided a comprehensive review of numerical modeling of FSW/FSSW. Different models have been developed for the investigations on the heat inputs, the material flows, and the force variations in FSW/FSSW. These models involve solving the equations of conservation of energy, mass, and momentum for steady-state conditions considering incompressible viscous flow. Researchers have used Eulerian [20, 21], Lagrangian [22], and Arbitrary Lagrangian-Eulerian (ALE) [23, 24] descriptions to modeling of FSW/FSSW. Nandan et al. [25] established a computational fluid dynamics (CFD) model to systematically study 3D viscoplastic material flow and the physical nature of heat transfer in FSW. Also, by the use of solid mechanic-based ALE model, Zhang and Zhang [23] directly showed the movements of the material particles and found the material flow rules in FSW.

Heat generation is a very important parameter in FSW/FSSW and has been widely discussed in published literatures. Mishra et al. [26] have provided a comprehensive review on heat generation during FSW/FSSW. Zhang and Zhang [20] have established a new Eulerian model based on solid mechanics and studied the power and the heat generations from pin side surface, pin tip surface, and shoulder contact surface in different rotating speeds. Results indicate that the ratio of the heat input powers from the pin and the shoulder keeps constant in different rotating speeds. Strain and strain rate are two other important parameters which have been calculated during FSW/FSSW using finite element modeling in previous investigations [20, 27]. In some studies, the researchers have predicted recrystallized grain growth during FSW/FSSW using finite element modeling. In one of them, Zhang and Wu [27] have investigated the effect of tool geometries on strain rate, temperature, and grain size in FSW of AA6061-T6. They have calculated Zener-Hollomon parameter which is a function of temperature and strain rate and can predict the final sizes of recrystallized grains. They have mentioned that the contribution from the temperatures is much more important than the one from the deformations. Also, the results of their study showed that by increasing the input heat, the final grain size increased because of increasing Zener-Hollomon parameter.

Considering the previous literature, most of the studies have been done on aluminum alloys and the effect of thermomechanical parameters, like temperature, strain, and strain rate on microstructure of TRIP steel, has not been investigated using finite element modeling. On the other hand, the effect of FSW/FSSW environment on microstructure and mechanical properties of TRIP steel joints has not been studied. Owing to this, in the present work, experimental joining and finite element modeling were used to investigate the effects of thermomechanical parameters. Therefore, six types of joining were fabricated experimentally under rotational speed of 900, 1350, and 1800 rpm and environments of air and water. Then, 3D fully coupled finite element model was used to obtain thermal history, strain, and strain rate distribution in similar conditions of experimental welding. Finally, using finite element results (thermal history and strain), microstructure observation (optical microscopy and scanning electron microscopy), and measurement of mechanical properties (tensile strength and microhardness), the effects of thermomechanical parameters and welding environment investigated.

2 Materials and methods

2.1 Experimental

2.1.1 Base metal

The chemical composition of TRIP steel contained 0.2 C, 1.68 Mn, 1.43 Si, 0.03 Cr, 0.01 Ni, 0.016 Al, and 0.009 S (wt.%). The steel was prepared as a 5-kg ingot in an air induction furnace. The cast ingot was forged and small blocks were cut from forged stock. These blocks were soaked at 1200 °C for 1 h, and hot rolled to a thickness of 4 mm. Hot rolled plates were annealed at 900 °C for 1 h to reduce the hardness for easier cold rolling. The hot-rolled air annealed steel plates were cold rolled to achieve a final thickness of 1.2 mm.

The temperatures of Ac_1 and Ac_3 were calculated using Thermo-Calc database [28] and the amount of 705 and 836 °C were obtained, respectively. To obtain the microstructure of TRIP steel a two-step heat treatment was conducted. The intercritical annealing was done at temperature 790 °C for 10 min. After intercritical annealing, steel quenched to temperature of 350 °C and was hold for 12 min at this temperature. Finally, the steel was quenched by water to room temperature.

2.1.2 FSSW

TRIP steel plates with the dimensions of 30 mm × 100 mm × 1.2 mm were prepared for lap shear tensile test and then friction stir spot welded at tool rotational speeds of 900, 1350, and 1800 rpm in both environment of air and water. Plunge depth, dwell time, and plunge rate were fixed at 2 mm, 2 s, and 0.2 mm/s, respectively. The experiment conditions are given in Table 1. A tool made of tungsten carbide (WC) with a 10-mm shoulder diameter, a 5-mm pin diameter, and a 1.9-mm pin length was used. Note, the WC tool exhibited no wear and high dimension stability after each FSSW weld. Also, a special fixture was designed and fabricated because of high forces which imposed to workpiece during welding. FSSW was conducted using a vertical milling machine. The fixture and experimental setup of welding are shown in Fig. 1.

To validate the results of finite element model, the thermal history and temperature distribution of samples which welded under rotational speed of 1350 rpm in both environments were recorded using K-type thermocouple. The specimen used for this test was made as single part by milling a plate with an initial thickness equal to 2.4 mm. For this purpose, at first, the specimen was prepared by milling and then was heat treated by two-stage heat treatment to obtain TRIP steel microstructure. The use of a single part component instead of two separated plates was chosen to avoid possible effects due to the thermal contact resistance between the plates and to guarantee proper and stable measurements of the temperatures during the tests. This solution was used for the thermal tests only, which means for a set of specimens that were not used for the mechanical characterization. Four holes having a diameter equal to 1 mm were executed on sample in the width direction (two on one side and two on the other one) at a specific distance from the specimen center. The geometry of specimen that was used for temperature recording during welding is represented in Fig. 2.

2.1.3 Microstructure observation and mechanical tests

Optical microscopy (OM) and field emission scanning electron microscopy (FE-SEM) were used for microstructure observation. For the OM and SEM investigations, the transverse cross sections of the joints were prepared according to the standard grinding and polishing procedures. The samples for investigation with SEM were etched in Nital 2 % for 2–3 s. For OM, various etchant are possible. It was obtained that the metabisulfite solution ($Na_2S_2O_3 \cdot H_2O$ 10 g + H_2O 100 ml) is the best etchant solution and all of the four phases can be determined using it. Using a metabisulfite solution as the etchant reveals the retained austenite, ferrite, and bainite/martensite phases in white, gray, and black contrast, respectively [29].

Microhardness measurements were performed with a microhardness tester equipped with a Vickers indenter, applying a load of 100 g. Hardness was measured along lines parallel to the sheet surface at a distance of 0.5 mm from the surface of the upper sheet.

Table 1 Experimental welding parameters

samples	Rotational speed (rpm)	Welding environment	Plunge depth (mm)	Dwell time (s)	Plunge rate (mm/s)	Tool material
1	900	Air	2	2	0.2	Tungsten carbide
2	1350					
3	1800					
4	900	Water				
5	1350					
6	1800					

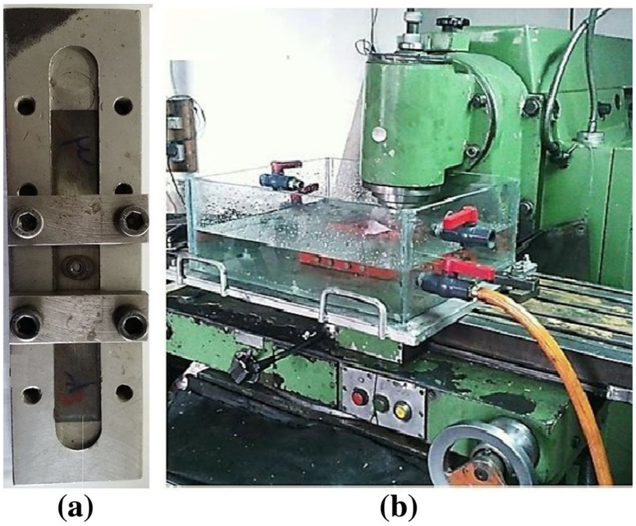

Fig. 1 **a** FSSW fixture and **b** underwater welding setup

The lap-shear tensile tests were conducted at room temperature on a computerized universal testing machine at a constant crosshead speed of $5 \times 10^{-2}\ \mathrm{s}^{-1}$. Two packing slices were adhesively joined to the weld specimen to ensure the axial loading of the test specimen. For each condition, three tensile tests were done and the average of obtained strengths was selected as the final strength. Also, fracture surfaces were investigated by FE-SEM micrograph.

2.2 Finite element model

In this work, the ABAQUS finite element modeling program was utilized, which has been previously used for FSW/FSSW simulations [11]. The geometry used in the simulations is shown in Fig. 3. The mesh is dense at the center of the workpiece to reduce hourglassing effect as depicted in Fig. 3. The element size is approximately 0.1 mm in the region surrounding the tool. The workpieces have been modeled using thermal-coupled element C3D8RT. This element type has 8-node tri-linear displacement and temperature degree of freedom and reduced integration with hourglass control.

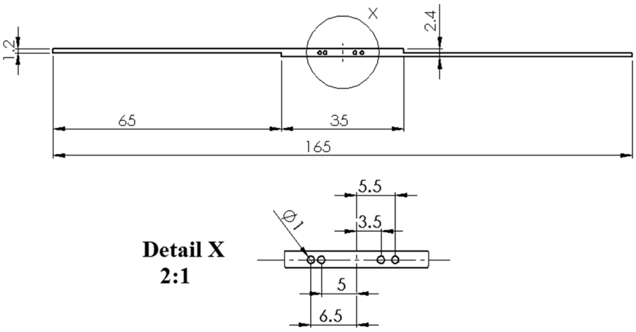

Fig. 2 Details of the specimens prepared for the thermal analysis

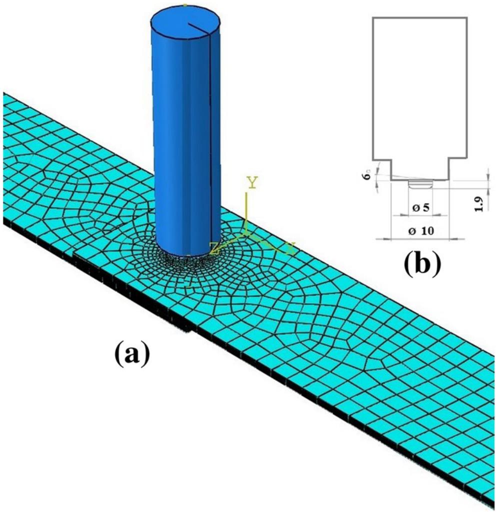

Fig. 3 **a** FSSW model geometry and mesh and **b** tool dimension

Since this work is not intended to study the mechanical responses of the tool, it was modeled as analytical rigid surfaces with prescribed motion at a reference node. The rigid body surfaces, however, carry thermal response, which are assumed as isothermal. The tool has a shoulder and an unthreaded pin as shown in Fig. 3. The diameters of the shoulder and the pin are 10 and 5 mm, respectively. The reference node was defined for the rigid body that has translation, rotation, and thermal degree of freedoms.

For simulating the FSSW, a 3D explicit fully coupled model was used. The describing equation of the heat transfer during welding is introduced as follows [30]:

$$\frac{\partial}{\partial \mathrm{x}}\left(\mathrm{k_x}\frac{\partial \mathrm{T}}{\partial \mathrm{x}}\right)+\frac{\partial}{\partial \mathrm{x}}\left(\mathrm{k_y}\frac{\partial \mathrm{T}}{\partial \mathrm{y}}\right)+\frac{\partial \mathrm{y}}{\partial \mathrm{x}}\left(\mathrm{k_z}\frac{\partial \mathrm{T}}{\partial \mathrm{z}}\right)+q \\ =\rho \mathrm{C}\frac{\partial \mathrm{T}}{\partial \mathrm{t}} \tag{1}$$

where x, y, and z describe the coordination in Cartesian system and ρ, C, k, T, t, and q are density, specific heat, conductivity, temperature, time, and generated heat, respectively.

In this study, it has been considered that the main source of the generated heat during FSSW is the friction between the tool and the sheets, and the plastic deformation of the specimens near the tool, as well. The generated heat by the friction (q_f) can be calculated using the following equation [30]:

$$q_f = 2\pi\mu RNF \tag{2}$$

where R, N, μ, and F are the distance from the tool axis, rotational speed, friction coefficient, and normal force, respectively. The friction coefficient assumed to be constant. The amount of 0.49 was reported in the previous studies for μ between similar materials [31]. In the simulation of tool penetration into the material, a constant plunge rate was used.

When the plunge rate is controlled, the plunging is done at a constant rate and the normal force is variable. In this study, the plunge depth was fixed at 0.25 mm/s (2 mm plunge depth in 8 s), and so, the normal force was variable during welding.

The heat generation by the plastic straining (q_p) assumed as follows:

$$q_p = \eta\tau\,\dot{\varepsilon} \tag{3}$$

Here, η, τ, and $\dot{\varepsilon}$ are the dissipated heat fraction due to deformation (between 0 and 1), the shear stress, and strain rate, respectively.

Some of the total heat generated at the shoulder/workpiece interface is transported into the tool material during FSSW. The ratio of the heat that enters the workpiece to the heat transported into the tool can be deduced from this formula [32]:

$$f = \frac{\sqrt{(k\rho C)_w}}{\sqrt{(k\rho C)_t}} \tag{4}$$

where $(k\rho C)_w$ and $(k\rho C)_t$ are obtained by multiplying the thermal conductivity (k), density (ρ), and specific heat capacity (C) of workpiece and tool materials, respectively. In the FSSW of similar TRIP steels, the temperature at the tool/workpiece interface is generally concentrated in the range of 800–1100 °C [33]. Therefore, the thermo-physical properties of the tool [31] and the workpiece [33] at 950 °C are substituted to Eq. 4, which leads to an *f* value of 0.81.

The in-air and underwater FSSWs have the same initial boundary conditions for the calculations of temperature fields:

$$T(x,y,z,t)|_{t=0} = T_0(x,y,z,t) = 25\,^{\circ}C \tag{5}$$

The convection boundary condition for all the surfaces of workpiece is

$$-k\frac{\partial T}{\partial y} = h(T-T_0) \tag{6}$$

Where k is the thermal conductivity and *h* is the convection coefficient.

In most of the previous studies, the surfaces of workpiece exposed to the atmosphere were allocated a convection coefficient of 10–30 W/(m^2 °C) for thermal modeling of in-air FSSW. Based on this, the convection coefficient is set to be 15 W/(m^2 °C) for the surfaces of the plates in this study.

Regarding the underwater FSSW, the heat dissipation conditions for all sides of the workpiece are different from those under air environment. For the top surface near welding tool, the contact water is in the boiling state under the effect of elevated temperature, leading to intense heat transfer between the workpiece and the boiling water. While for the other surfaces exposed to the non-boiling water, the heat is dissipated from the workpiece by natural convection of water. It is reported that the convection coefficients of non-boiling and boiling water are, respectively, about 850 and 3000 W/(m^2 °C) [30].

By employing the Arbitrary Lagrangian-Eulerian (ALE) formulation, large deformations can be simulated by remeshing. In ALE formulation, the main point is to control the distortion of the elements by improving the aspect ratio of the distorted elements [34]. More details about ALE formulation are available in Belytschko et al. [34]. The temperature-dependent properties of studied steel were given in the authors' previous work which was done at simulation of FSSW of TRIP steel [33].

3 Results and discussion

3.1 FEM validating

Figure 4 shows the temperature, strain and strain rate distribution at the case 1350 rpm which were obtained at the end of dwell time (for temperature) and end of the cooling (for strain and strain rate). In Fig. 5a, the thermal history of a point near the tool pin in case in-air welded at 1350 rpm of rotational speed has been validated with experimentally obtained result for this point. Also, Fig. 5b shows the comparison between numerical and experimental peak temperatures, in cases which welded under rotational speed of 1350 rpm. The maximum peak temperatures of the in-air welds are 912, 1040, and 1120 °C, while those of the underwater joints are 760, 866, and 995 °C. As shown from Fig. 5, finite element results are in a good agreement with results that have been recorded by thermocouples.

Also, according to the finite element results, the maximum achieved strains in the in-air cases are 7.2, 8.4, and 9.9 when the maximum strains imposed by welding process in underwater joints are 6.1, 6.9, and 8.2. The strain rates were more dependent to the rotational speed. The values of strain rate for in-air cases were 8.9, 9.8, and 10.1, and for underwater cases, the values were 8.7, 9.7, and 10.2. In the preceding studies, the stated range of the reported strain and strain rate are too wide. From the other point of view, in the investigations with comparable condition of the present work, the data are reported in the range of 1–10 for strain and 2–15 for strain rate [17–19].

Figure 6 represents the normal force history for case 1350 rpm during simulation. When the pin touches the surface of the workpiece because of the material resistance against strain, force starts to increase until the force reaches to a maximum at a value of 6 KN. As pin penetration continues, the temperature increases due to the frictional heating and the material plasticizes; its resistance decreases and there is a drop in the force value. The tool axial displacement causes the upward movement of the material, like a reverse extrusion. When the shoulder touches this extruded material, force value

Fig. 4 Temperature, strain, and strain rate distribution in sample welded at 1350 rpm and air environment

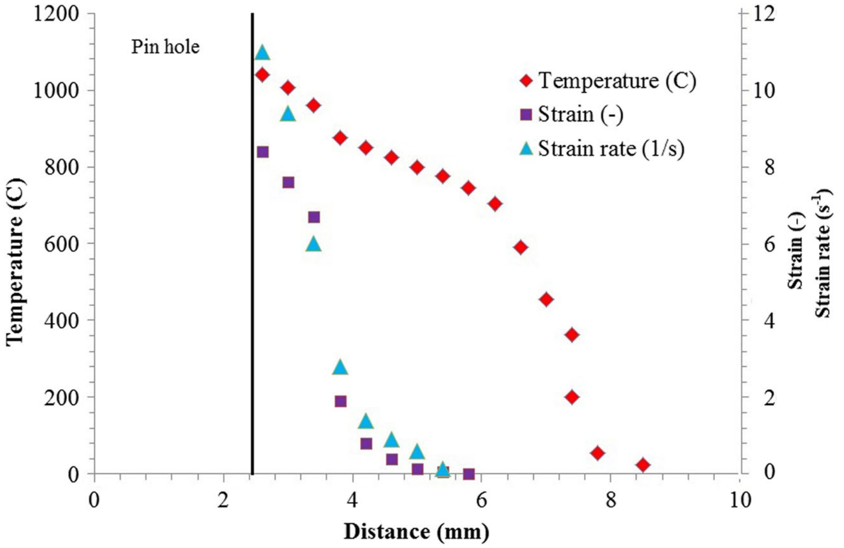

increases again due to the “forging force” produced by the shoulder. Immediately before the dwell period, where the tool remains rotating but there is no axial displacement, the force reaches another peak 12 KN. During dwell time, there is a drop in force value because of the low resistance of the material being deformed due to the frictional heating. Mazzaffero et al. [9] have measured the amount of normal force during FSSW of TRIP steel which was same to material of present study. The finite element results of this study can be validated with their results.

3.2 Microstructure and mechanical properties

Figure 7 shows the section view of in-air FSSWed sheets under rotational speed of 1350 rpm which four zones can be determined by various colors observation. As reported previously in the FSSW of TRIP steel joints [3, 9], the FSSWed TRIP joint was classified as four zones, the stir zone (SZ), thermomechanically affected zone (TMAZ), high temperature heat-affected zone (HTHAZ), and low temperature heat-affected zone (LTHAZ). Figure 8 shows the section views of the finite element models, which indicate the distribution of temperature and strain in all the cases. In this figure, the welded zone in each case subdivided to four zones according to temperature distribution and maximum strain; SZ, where the temperature increases above Ac_3 $(836\,^{\circ}C)$ and the large amount of strain and strain rate leads to the stirring of the sheets; TMAZ, where the temperature is between Ac_3 and Ac_1 $(705\,^{\circ}C\ )$ with mediocre or low strain; HTHAZ, where the high temperature rises above Ac_1 but stays under Ac_3 and there is no deformation and LTHAZ, where the temperature is less than Ac_1. The minimum temperature at LTHAZ assumed to be 300 ˚C which no considerable transformation occurred in lower temperatures.

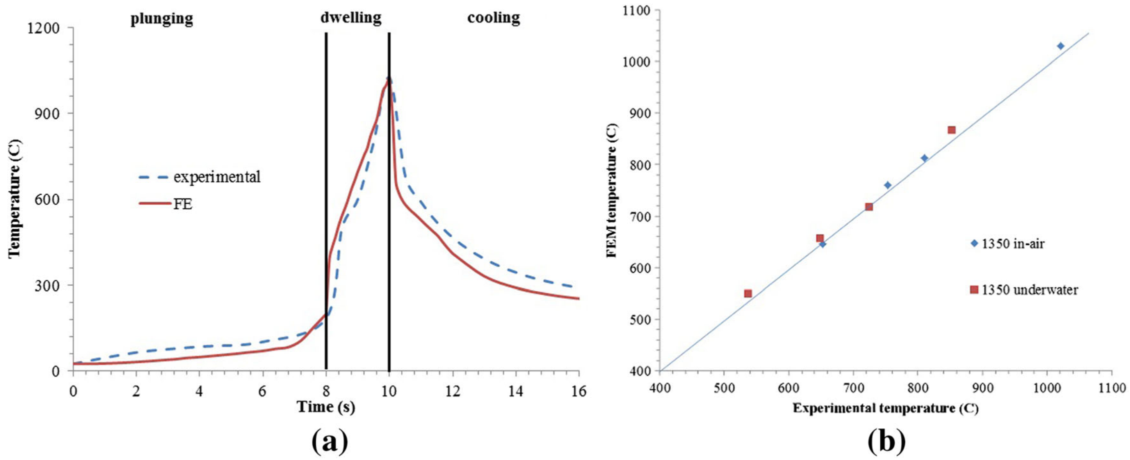

(a) (b)

Fig. 5 **a** Thermal history for point from SZ of 1350 in-air weld which compared with thermal history of similar point in FE model and **b** comparison between numerical and experimental peak temperatures, in cases which welded under rotational speed of 1350 rpm. The data were obtained at the end of dwell time and distances of 3.5, 5, 5.5, and 6.5 mm from the pin center

Fig. 6 Normal force and plunging histories during FSSW of sample welded in air and 1350 rpm

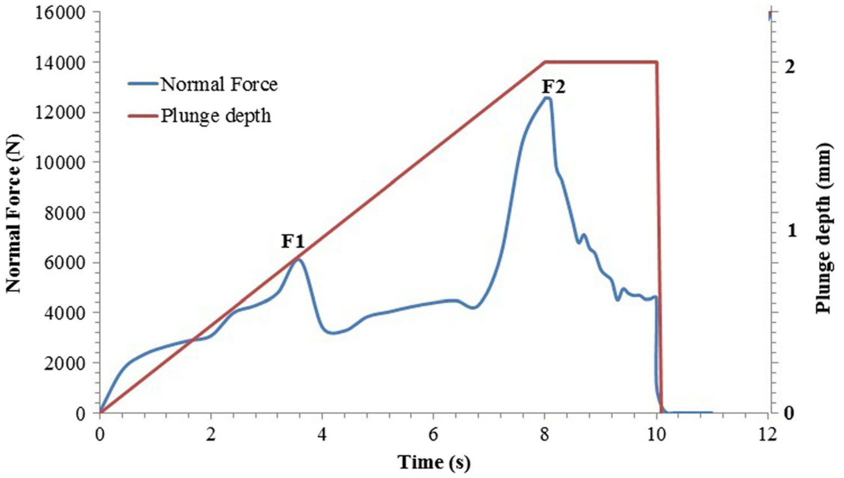

Figure 9 represents the FE-SEM micrographs of base metal and subdivided welding zones.

As is clear from Fig. 9a, the ferrite grains are the major phase of base metal (BM). Austenite and martensite grains were determined by smooth and rough appearance, respectively. Retained austenite grains appear in two morphologies: blocks and films. Bainite is clearly seen as the regions with lamellar structure consisting of bainitic ferrite and retained austenite. Similar observations have been reported in previous studies [35]. The microhardness of sample is shown in Fig. 10. The base metal has an average microhardness of 250 VHN.

Figure 9b shows the microstructure of LTHAZ. It is difficult to identify a difference between base metal and this zone, but focusing on both microstructure clarify that the morphology of retained austenite in LTHAZ changed comparing base metal by growing the bainitic ferrite as lamellar grains into austenite grains (black ellipses in figure). By growing the bainitic ferrite, carbon is amassed into the nearing austenite lamellae, thus, enriching the retained austenite lamellae with carbon [36, 37]. It is similar to bainitic isothermal transformation step of two-stage heat treatment of TRIP steel processing which achieved about 350 ˚C in this case. It can be concluded that the temperature was less than Ac_1 in LTHAZ. This conclusion was confirmed by temperature recording previously. A temperature less than Ac_1 has been caused to tempering of martensite which was in the base metal, and therefore, decreased the microhardness of this zone comparing base metal well (Fig. 10) [38].

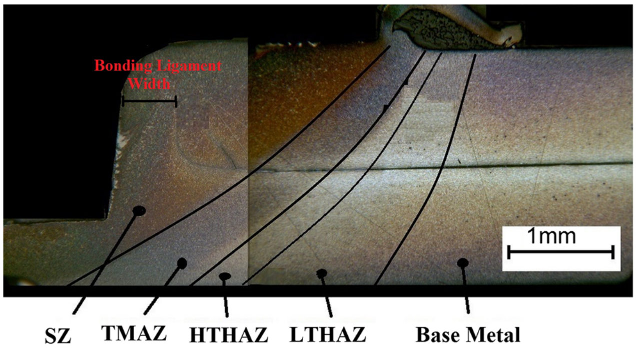

Fig. 7 The section view of in-air weld that joined under rotational speed of 1350 rpm

The micrograph of HTHAZ in Fig. 9c shows that amount of martensite phase increased. Where TRIP steel is heated up to temperatures between Ac_1 and Ac_3, austenite and ferrite are in equilibrium. During cooling, some of austenite grains transformed to martensite, and therefore, the microhardness of region increased to average amount of 400 VHN, which is higher comparing base metal and LTHAZ. Figure 11 compares the HTHAZ zones at cases 1350 rpm in both environments. HAZ of underwater joint include finer ferrite grains because of the lower temperature and rapid cooling rate. Also, the amount of martensite in underwater case is higher comparing in-air joint. In fact, the prior austenite grain size in underwater joint is smaller because of the lower peak temperature but almost all of the austenite grains transform to martensite because of higher cooling rate. This observation explains the higher microhardness of HAZ in the underwater cases.

From the Fig. 9d, it is obvious that the microstructure of TMAZ are composed by ferrite, austenite, bainite, and martensite which indicates that the material was heated to peak temperature between Ac_3 and Ac_1, where new austenite grains have formed. During cooling, some austenite grains transforms into bainite and martensite. Also, the microstructure in TMAZ seems to be lightly deformed as a result of moderate deformation imposed by the process in this zone. According to Fig. 10, the microhardness increased comparing previous zones because of high amount of martensite.

Xu et al. [39] reported that recrystallized grains formed during the FSW grow very rapidly during the weld cooling cycle commonly known as the post annealing effect. In the TMAZ and HAZ, the morphology of the grains significantly changed from equiaxed to a finer elongated shape under rapid

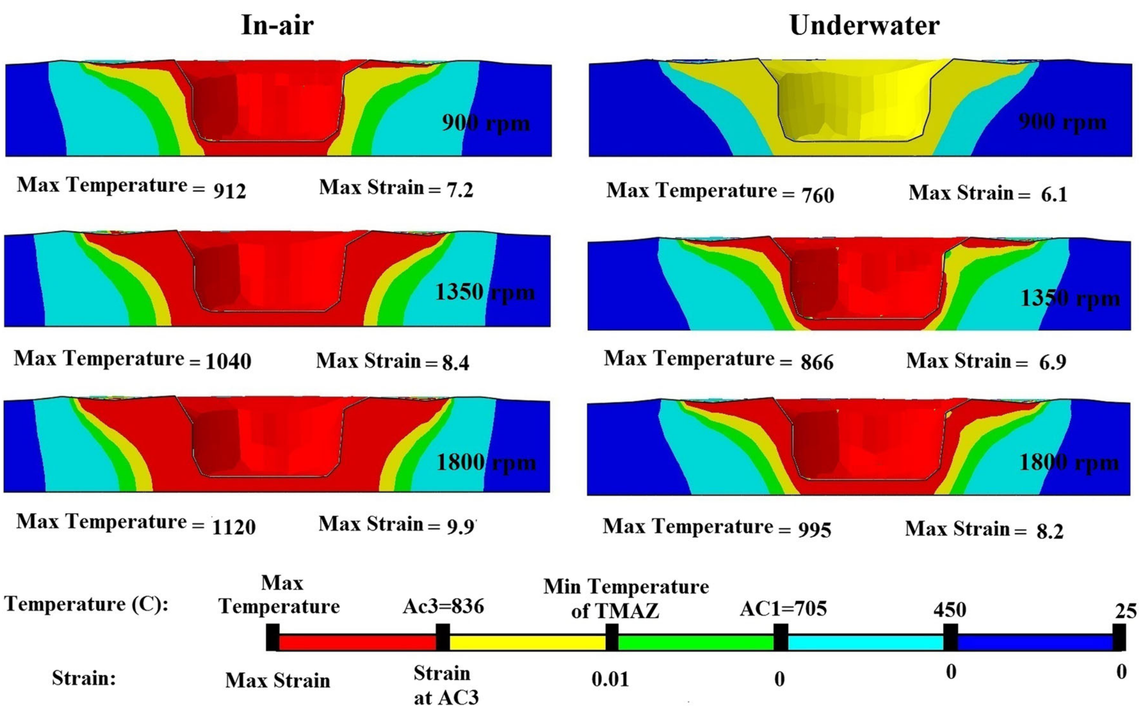

Fig. 8 The section views of finite element models that indicate temperature and strain distribution in all case at the end of dwell time

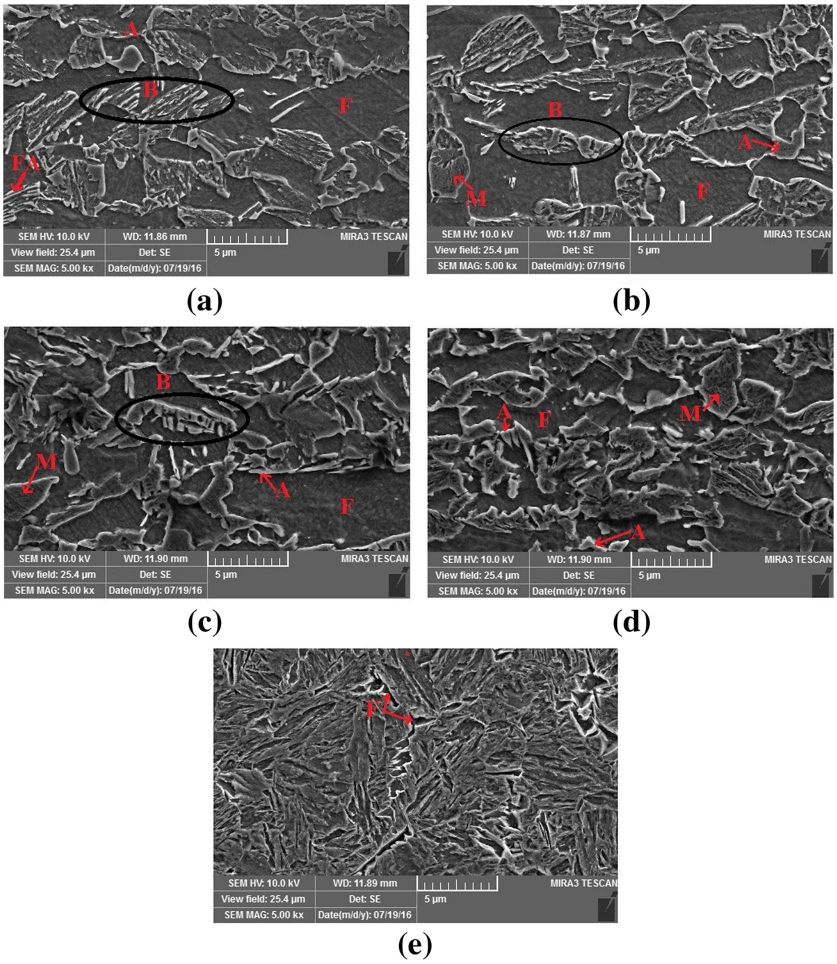

(a) (b) (c) (d) (e)

Fig. 9 FE-SEM micrographs of sample welded in air and 1350 rpm: **a** BM, **b** LTHAZ, **c** HTHAZ, **d** TMAZ, and **e** SZ

Fig. 10 Vickers microhardness profiles of the six welded samples

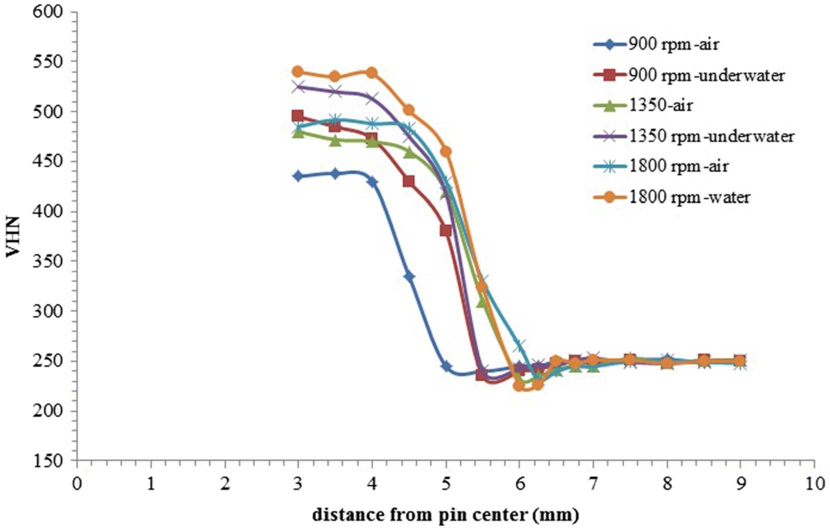

cooling. This result suggested that the online rapid cooling can be thought of as a way to possibly eliminate the post annealing effect. According to finite element results in Fig. 8, the total sizes of deformed zones (SZ + TMAZ) are reduced in underwater joints. In fact, a decrease in the input heat causes a significant decrease in plastic deformation during underwater welding.

The microstructure of SZ is shown in Fig. 9e. The major phase in microstructure is martensite and the average microhardness of 550 VHN confirms this observation. However, some ferrite and widmanstatten ferrite grains can be seen. During welding the temperature of SZ is rose above Ac_3 and microstructure completely changes to austenite. Because of high temperature and intense strain and strain rate imposed by the process the occurring of discontinues dynamic recrystallization (DDRX) of austenite is possible.

Figure 13 plots the time-temperature history profiles of SZs of all joints. As the tool rotates, the temperatures of SZs of in-air joints are gradually increased to the peak value and then show a slow cooling rate. While for the underwater joints, the peak temperatures are all lower than the corresponding value of the in-air joints. In addition, the thermal cycle exhibits larger cooling rates.

Figure 12 compares the FE-SEM micrographs of the SZ of cases 1350 rpm in both environments. According to this figure microstructure of underwater joint includes martensite, bainite and a considerable amount of widmanstatten ferrite and also recrystallized ferrite grains that indicate the temperature was slightly lower than Ac_3.

According to finite element outputs, in 900 rpm underwater joint the stir zone has not formed because the maximum temperature was just a little more than Ac_1. Also, a very narrow SZ has formed in 1350 rpm underwater joint. The peak temperature in 1800 rpm underwater joint is sufficiently higher than Ac_3 and a considerable SZ formed.

It is clear from Fig. 8, the high-temperature distributing areas in underwater joints are remarkably narrowed and the amounts of strains are reduced in contrast to the in-air joints.

Fig. 11 Optical microstructure of HTHAZ at samples FSSWed at 1350 rpm: **a**in-air and **b** underwater (*F* ferrite, *M* martensite)

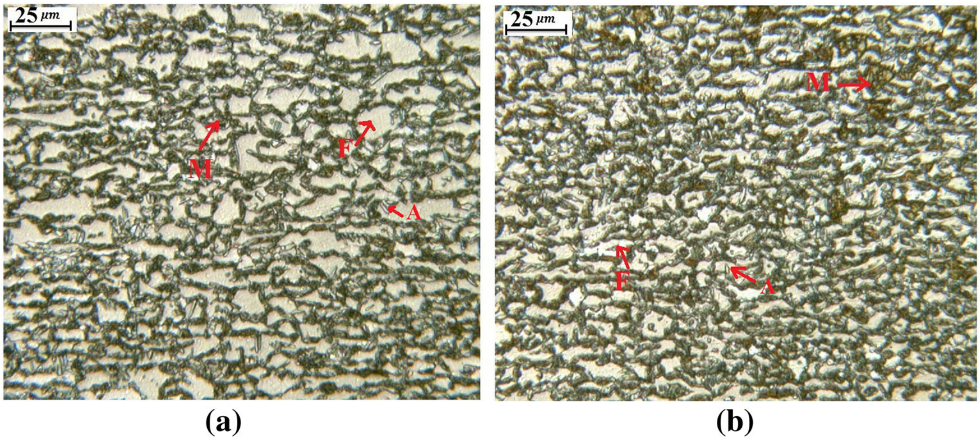

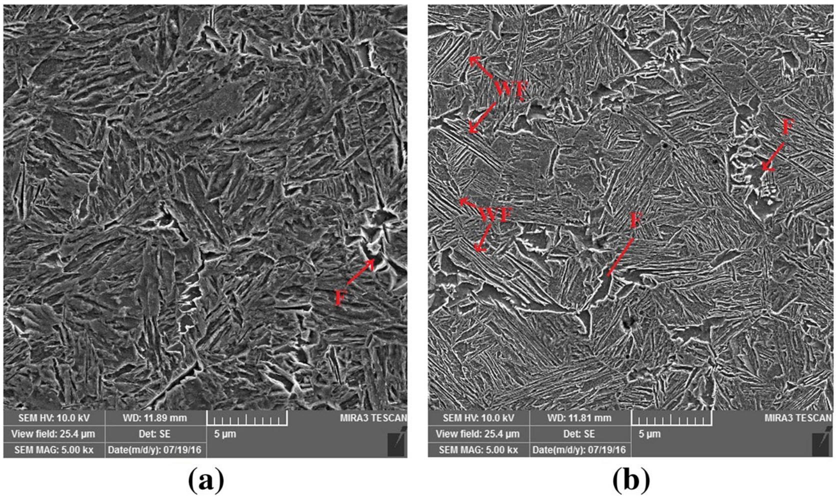

Fig. 12 FE-SEM micrographs of SZ at samples FSSWed at 1350 rpm: **a** in-air and **b** underwater (*F* ferrite, *WF* widmanstatten ferrite)

Figure 10 shows the hardness profiles over the various zones in the six samples. Microhardness at SZs is higher with respect to base alloy in all cases. The improvement was attributed to the combined effect of fine grain size and appearance of martensite at SZs. Average microhardness of 490 VHN at SZ was reported by mazzaferro et al. [9] for FSSWed TRIP steel with similar composition of present study. The peak hardness of welds obtained in air and water environment in this study are 510 and 550 VHN, respectively. It is observed that microhardness of sample joined under 900 rpm in air is lower significantly from the two other samples because of low heat generation and low cooling rate which caused soft microstructure. Also, the average hardness in the SZs of underwater joints is about 40 VHN higher than the SZs of the in-air joints. Such an enhancement in average hardness is directly related to the formation of the fine grains and harder phases under rapid cooling. These tendencies well follows the change of the microstructure distributions in both joints.

Microhardness of TMAZ decreases comparing SZ because of reduction in martensite fraction of microstructure. Decreasing of microhardness is continued by transition to HTHAZ but still the VHN is above comparing base metal. According to Fig. 10 hardness of LTHAZ at in-air joints is less than BM. As was said before, a temperature below Ac_1 may also induce tempering of the martensite, which is present in the BM before welding; this will lead to decreased hardness as well [38].

The strength of the weld emanates from the region where the two sheets are joined, which is commonly known as the bonding ligament width (Fig. 7). It was reported [3, 6] that not only the bonding ligament width is responsible for the strength, but also the type of microstructure developed in the bonding ligament. The results of the lap shear tensile tests for cases are given in Fig. 14. The results of in-air joints show an increasing at 900 to 1350 rpm which is followed by a decreasing at 1350 to 1800 rpm. By increasing the rotational speed,

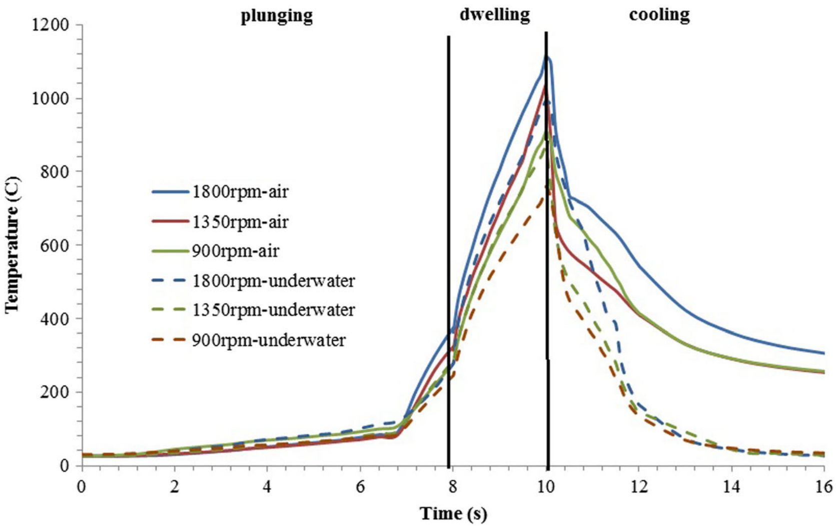

Fig. 13 Thermal histories of SZs in all samples

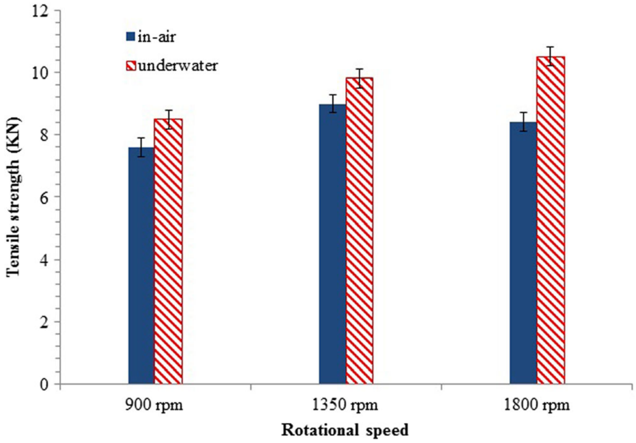

Fig. 14 Tensile strength of in-air and underwater joints

the strain rate and input heat increase and cause to more stirring in the SZ. The Zener-Hollomon parameter (Z) can be used to prediction of recrystallized prior austenite grain size (d) as follows [40]:

$$Z = \dot{\varepsilon}\, EXP\left(\frac{Q}{RT}\right) \tag{5}$$

$$d = k\left(\frac{Z}{A}\right)^{-p} \tag{6}$$

Where $\dot{\varepsilon}$, Q, and T are strain rate (s^{-1}), activation energy (J/Mol), and absolute temperature (°K). R is the constant and equal to 8.314 ($\frac{J}{{}^{\circ}K\,Mol}$). Also, k and p are dependent on material properties and their values for TRIP steels with similar chemical composition of TRIP steel studied in this paper were reported in [41]. According to the finite element results, the value of strain rate increases by increasing the rotational speed. By increasing the strain rate, the amount of Z parameter increases, and therefore, the grain size of prior austenite decreases. It has been reported that by decreasing the prior austenite grain size, the packet size of lath martensite, which will be formed from austenite, decreases, and therefore, the strength of microstructure increases [42]. However, when the rotational speed is too high (1800 rpm in this study), the negative effect of temperature rising overcomes to positive effect of strain rate and the Z parameter decreases, which causes to grain growth of prior austenite. Therefore, the strength of microstructure reduced because of formation of lath martensite with large packets. In joints welded in air, by increasing the rotational speed, the strength is increased from 7.6 KN at 900 rpm to a maximum value of 9 KN at 1350 rpm and then decreased to 8.4 KN at 1800 rpm. When the environment of the welding is replaced by water, increasing the rotational speed, increases the strain rate, but the temperature rising is limited because of more and fast heat transfer between material and water. According to Fig. 14, the strengths of the underwater welds are higher than the in-air welds at all rotational speeds. Also, in underwater welds, the strength increases from 8.5 KN at 900 rpm to 10.5 KN at 1800 rpm. As a result of limiting the heat input and also decreasing the amount of time, the alloy stays above a certain

Fig. 15 FE-SEM micrographs of tensile shear fracture surface appearance of FSSWed TRIP steel **a** 900 rpm, in-air; **b** 1350 rpm, in-air; **c** 1800 rpm, in-air; **d** 900 rpm, underwater; **e** 1350 rpm, underwater; and **f** 1800 rpm, underwater

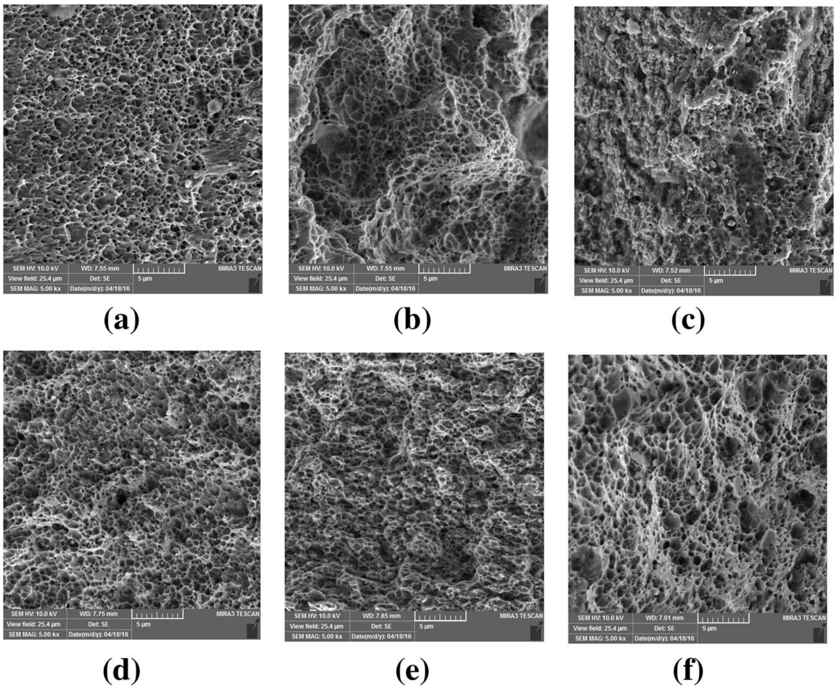
(a) (b) (c)
(d) (e) (f)

temperature, grain growth is impeded, and this renders the underwater welded joints stronger.

The fracture surfaces of the joints are illustrated in Fig. 15. It can be seen from Fig. 15 that the fracture surface of the 900 rpm in-air weld shows a ductile fracture with uniform dimple sizes while that of the 1350 rpm in-air weld displays a deeper dimple pattern. In the case of the joint welded at 1800 rpm, the fracture surface is somewhat different from other joints where it does not reveal a dimple pattern. For this joint, the fracture is less ductile which agrees with lower tensile elongation of it. On the other hand, the fracture surface of the underwater joints exhibits only a dimple pattern which predominantly shows ductile fracture. In addition, for the underwater joints, the sizes of the dimples were uniform, and the dimple size increased with increasing rotational speed.

4 Conclusions

- Finite element modeling with ALE description was used to simulation FSSW of 0.2C + 1.43Si + 1.68Mn TRIP steel sheets in air and water environments. Temperature, strain, and strain rate were obtained and the results were validated by experimental results.
- Experimental joining was done at six samples and in the same conditions of the finite element simulations (under rotational speed of 900, 1350, and 1800 rpm at air and water environments). Also, the microstructure and mechanical properties of joints were studied.
- Section view of FSSWed sample showed that for different zones formed in welding area: SZ, TMAZ, LTHAZ, and HTHAZ. These subdivided zones were determined in finite element models using strain and temperature distributions.
- The finite element results showed that by increasing the rotational speed the values of temperature and strain increased in both environments. Also, SZ + TMAZ sizes were smaller in underwater samples because of lower temperature and strain.
- By increasing of the rotational speed at in-air joints, the lap shear tensile strength of the joints increased up to a maximum value of 9.1 KN in rotational speed of 1350 rpm and then decreased. By increasing the rotational speed and so strain rate, the amount of Zener-Hollomon parameter increases, and therefore, the grain size of prior austenite decreases. This decreases the packet size of lath martensite and the strength is improved. However, when the rotational speed is too high (1800 rpm in this study), the negative effect of temperature rising overcomes to positive effect of strain rate and the Z parameter decreases.
- In water environment, the strain rate is similar to in-air welding, but the temperature is lower. Therefore, the Z parameter decreases by increasing rotational speed continuously and the final microstructure is finer. This explains the higher strength of underwater joints.
- The fracture surfaces of joints showed a dimple pattern ductile fracture in all cases except 1800 rpm in-air joint that the fracture was less ductile which agrees with lower tensile elongation of it.

References

1. Militzer M (2002) A synchrotron look at steel. Science 298:975–976
2. Jacques PJ, Ladriere J, Delannay F (2001) On the influence of interactions between phases on the mechanical stability of retained austenite in transformation-induced plasticity multiphase steels. Metall Mater Trans A-Phys Metall Mater Sci 32:2759–2768
3. Lomholt TC, Adachi Y, Peterson J, Steel R, Pantleon K, Somers MA (2011) Microstructure characterization of friction stir spot welded TRIP steel. Adv Mater Res 409:275–280
4. WM Thomas, ED Nicholas, JC Needham, MG Murch, P Temple-Smith, CJ Dawes (1991) Friction-stir butt welding. UK Patent
5. Hsieh MJ, Chiou YC, Lee RT (2015) Friction stir spot welding of low-carbon steel using an assembly-embedded rod tool. J Mater Process Technol 224:149–155
6. Ahmed M, Ahmed E, Hamada A, Khodir S, Seleman ME-S, Wynne B (2016) Microstructure and mechanical properties evolution of friction stir spot welded high-Mn twinning-induced plasticity steel. Mater Des 91:378–387
7. Joy-A-Ka S, Ogawa Y, Sugeta A, Sun Y, Fujii H (2014) Fatigue fracture mechanism on friction stir spot welded joints using 300 MPa-class automobile steel sheets under constant and variable force amplitude. Procedia Mater Sci 3:537–543
8. Sun Y, Fujii H, Takaki N, Okitsu Y (2012) Microstructure and mechanical properties of mild steel joints prepared by a flat friction stir spot welding technique. Mater Des 37:384–392
9. Mazzaferro C, Rosendo T, Tier M, Mazzaferro J, Dos Santos J, Strohaecker T (2015) Microstructural and mechanical observations of galvanized TRIP steel after friction stir spot welding. Mater Manuf Process 30:1090–1103
10. Nandan R, DebRoy T, Bhadeshia H (2008) Recent advances in friction-stir welding–process, weldment structure and properties. Prog Mater Sci 53:980–1023
11. He X, Gu F, Ball A (2014) A review of numerical analysis of friction stir welding. Prog Mater Sci 65:1–66
12. Heidarzadeh A, Jabbari M, Esmaily M (2015) Prediction of grain size and mechanical properties in friction stir welded pure copper joints using a thermal model. Int J Adv Manuf Technol 77:1819–1829
13. S Rouhi, A Mostafapour, M Ashjari (2015) Effects of welding environment on microstructure and mechanical properties of friction stir welded AZ91C magnesium alloy joints. Sci Technol Welding Joining 1362171815Y. 0000000058
14. Imam M, Ueji R, Fujii H (2016) Effect of online rapid cooling on microstructure and mechanical properties of friction stir welded medium carbon steel. J Mater Process Technol 230:62–71
15. Fratini L, Buffa G, Shivpuri R (2009) In-process heat treatments to improve FS-welded butt joints. Int J Adv Manuf Technol 43:664–670
16. Farrokhi H, Heidarzadeh A, Saeid T (2013) Frictions stir welding of copper under different welding parameters and media. Sci Technol Weld Join 18:697–702

17. Nourani M, Milani AS, Yannacopoulos S (2012) On the Experimental and Numerical Predictions of Strain during Friction Stir Welding: A Case Study on 7050 Aluminum Alloy. Trans Control Mech Syst 1:259–263
18. ZW Chen, S Cui (2009) Strain and strain rate during friction stir welding/processing of Al-7 Si-0.3 Mg alloy. IOP Conference Series Materials Science and Engineering vol. 4, ed, p. 012026
19. Arora A, Zhang Z, Deb A, DebRoya T (2009) Strains and strain rates during friction stir welding. Scr Mater 61:863–866
20. Zhang Z, Zhang H (2014) Solid mechanics-based Eulerian model of friction stir welding. Int J Adv Manuf Technol 72:1647–1653
21. Feulvarch E, Roux J-C, Bergheau J-M (2013) A simple and robust moving mesh technique for the finite element simulation of friction stir welding. J Comput Appl Math 246:269–277
22. Tutunchilar S, Haghpanahi M, Givi MB, Asadi P, Bahemmat P (2012) Simulation of material flow in friction stir processing of a cast Al–Si alloy. Mater Des 40:415–426
23. Zhang Z, Zhang H (2008) A fully coupled thermo-mechanical model of friction stir welding. Int J Adv Manuf Technol 37:279–293
24. Pan W, Li D, Tartakovsky AM, Ahzi S, Khraisheh M, Khaleel M (2013) A new smoothed particle hydrodynamics non-Newtonian model for friction stir welding: process modeling and simulation of microstructure evolution in a magnesium alloy. Int J Plast 48: 189–204
25. Nandan R, Roy GG, Lienert TJ, Debroy T (2007) Three-dimensional heat and material flow during friction stir welding of mild steel. Acta Mater 55:883–895
26. RS Mishra, PS De, N Kumar (2014) Friction stir processing: Springer
27. Zhang Z, Wu Q (2015) Numerical studies of tool diameter on strain rates, temperature rises and grain sizes in friction stir welding. J Mech Sci Technol 29:4121–4128
28. JO Andersson, T Helander, L Höglund, PF Shi, B Sundman (2002) Thermo-Calc, ed: Calphad. Comp Tools Mater Sci 26
29. Girault E (1998) Metallographic methods for revealing the multiphase microstructure of TRIP-assisted steels. Mater Charact 40: 111–118
30. Zhang H, Liu H, Lei Y (2013) Thermal modeling of underwater friction stir welding of high strength aluminum alloy. Trans Nonferrous Metals Soc China 23:1114–1122
31. Manvatkar V, De A, Svensson L-E, DebRoy T (2015) Cooling rates and peak temperatures during friction stir welding of a high-carbon steel. Scr Mater 94:36–39
32. Bastier A, Maitournam M, Van Dang K, Roger F (2006) Steady state thermomechanical modelling of friction stir welding. Sci Technol Weld Join 11:278–288
33. A Mostafapour, A Ebrahimpour, T Saeid (2016) Finite element investigation on the effect of FSSW parameters on the size of welding subdivided zones in TRIP steels. Int J Adv Manuf Technol 1–13
34. T Belytschko, WK Liu, B Moran, K Elkhodary (2013) Nonlinear finite elements for continua and structures: Wiley
35. Shena YF, Qiu LN, Sun X, Zuo L, Liawc PK, Raabe D (2015) Effects of retained austenite volume fraction, morphology, and carbon content on strength and ductility of nano structured TRIP-assisted steels. Mater Sci Eng A 636:551–564
36. Girault E, Mertens A, Jacques P, Houbaert Y, Verlinden B, Humbeeck JV (2001) Comparison of the effects of silicon and aluminium on the tensile behaviour of multiphase TRIP-assisted steels. Scripta Mater 44:885–892
37. Lomholt TC (2011) Microstructure evolution during friction stir spot welding of TRIP steel, Ph.D, Department of Mechanical Engineering. Technical University of Denmark, Denmark
38. AK Sinha (2002) Physical metallurgy handbook: McGraw-Hill
39. Xu N, Ueji R, Fujii H (2014) Enhanced mechanical properties of 70/30 brass joint by rapid cooling friction stir welding. Mater Sci Eng A 610:132–138
40. Zhu L-J, Di W, Zhao X-M (2007) Recrystallization modelling of hot deformed Si-Mn TRIP steel. J Iron Steel Res Int 14:61–65
41. Medina SF, Hernandez CA (1996) Modelling of the dynamic recrystallization of austenite in low alloy and microalloyed steels. Acta Mater 44:165–171
42. J Hidalgo, MJ Santofimia (2016) Effect of prior austenite grain size refinement by thermal cycling on the microstructural features of as-quenched lath martensite. Metall Mater Trans A 1–14